Nanoscale

Accepted Manuscript

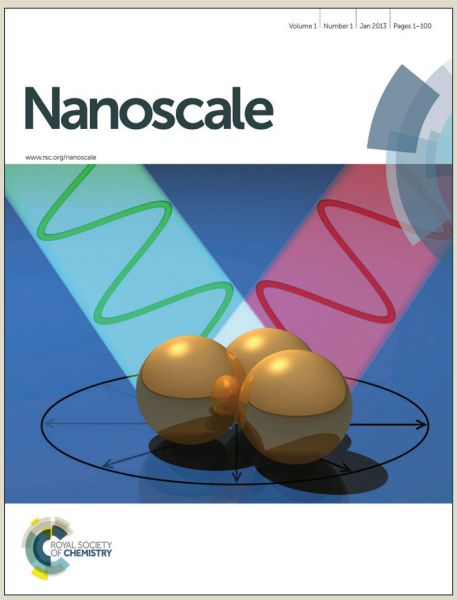

ROYAL SOCIETY OF CHEMISTRY

www.rsc.org/nanoscale

Nanoscale

PAPER

Relationships among structural topology, bond strength, and mechanical properties of single-walled aluminosilicate nanotubes

Received 00th January 20xx,
Accepted 00th January 20xx

DOI: 10.1039/x0xx00000x

www.rsc.org/

Kai-Hsin Liou,[a] Nien-Ti Tsou[b] and Dun-Yen Kang*[a]

Carbon nanotubes (CNTs) are regarded as small but strong due to their nanoscale microstructure and high mechanical strength (Young's modulus exceeds 1000 GPa). A longstanding question has been whether there exist other nanotube materials with mechanical properties as good as those of CNTs. In this study, we investigated the mechanical properties of single-walled aluminosilicate nanotubes (AlSiNTs) using a multiscale computational method and then conducted a comparison with single-walled carbon nanotubes (SWCNTs). By comparing the potential energy estimated from molecular and macroscopic material mechanics, we were able to model the chemical bonds as beam elements for the nanoscale continuum modeling. This method allowed for simulated mechanical tests (tensile, bending, and torsion) with minimum computational resources for deducing their Young's modulus and shear modulus. The proposed approach also enabled the creation of hypothetical nanotubes to elucidate the relative contributions of bond strength and nanotube structural topology to overall nanotube mechanical strength. Our results indicated that it is the structural topology rather than bond strength that dominates the mechanical properties of the nanotubes. Finally, we investigated the relationship between the structural topology and the mechanical properties by analyzing the von Mises stress distribution in the nanotubes. The proposed methodology proved effective in rationalizing differences in the mechanical properties of AlSiNTs and SWCNTs. Furthermore, this approach could be applied to the exploration of new high-strength nanotube materials.

Introduction

Nanotubes are essential building blocks in nanotechnology. Over the past two decades, nanotubes have attracted considerable attention, due to their one-dimensional geometry and unique properties, such as high mechanical strength, light weight, and high thermal and electrical conductance.[1-3] Since the discovery of carbon nanotubes (CNTs),[4] which is perhaps the most widely studied nanotube material, CNTs have been broadly applied to composite materials,[5,6] biomedical sensors,[7-9] medical imaging and photothermal therapy,[10-12] electrocatalyst,[13,14] electrochemical devices,[15] hydrogen detection and storage,[16,17] water harvesting,[18] and microelectronics.[19-24] The mechanical properties of CNTs is particularly noteworthy. Specifically, experimental[25-29] and computational[30,31] studies have determined that the Young's modulus of CNTs exceeds 900 GPa with a shear modulus of up to 478 GPa. Thus, CNTs are widely considered a small but strong material. Among existing nanomaterials, only graphene possesses mechanical strength comparable to that of CNTs.[32,33]

The excellent mechanical properties of CNTs make them a promising reinforcing filler material for nanocomposites;[5,6] however, developing an inexpensive means of mass producing high-purity monodispersed CNTs remains a challenge. Thus far, this has greatly limited their applicability in large-scale systems and devices. This situation has led to the development of metal oxide nanotubes, which can be synthesized under hydrothermal or solvothermal conditions, as an alternative to CNTs. In particular, single-walled aluminosilicate nanotubes (AlSiNTs), also known as the synthetic imogolites, have been attracting considerable attention.[34-41] AlSiNTs consist of a crystalline structural topology comprising $(HO)_3Al_2O_3SiOH$ with high monodispersity in terms of pore size (Fig. 1). Since

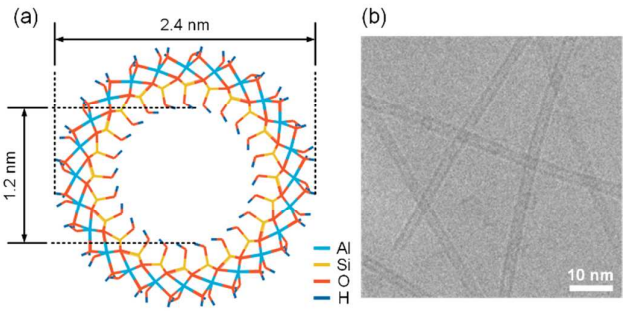

Fig. 1 (a) Cross-section of AlSiNT12 (12 denotes the number of unit cells around the circumference) and (b) cryo-TEM image of as-synthesized AlSiNTs.

[a] *Department of Chemical Engineering, National Taiwan University, No. 1, Sec. 4, Roosevelt Road, Taipei 10617, Taiwan. E-mail: dunyen@ntu.edu.tw*
[b] *Department of Materials Science and Engineering, National Chiao Tung University, No. 1001, University Road, Hsinchu 30010, Taiwan*

† Electronic Supplementary Information (ESI) available: The convergence test used in DFT calculation and the validation of the assumption of negligible Poisson effect can be found in the ESI, along with illustrations of total strain energy and the reaction force response of carbon-carbon, Al-O, and Si-O beam elements, von Mises stress and χ distributions of AlSiNT14 and 16, potential energy types, and boundary conditions in the simulations. The .mol files of AlSiNT models with various diameters are also appended. See DOI: 10.1039/x0xx00000x

2007, research has indicated that AlSiNTs possess very good mass transport[42-44] and catalytic properties.[45,46] The external surface of CNTs generally requires modification before being incorporated to another material for the fabrication of composites; however, the hydroxyl groups on the outer surface of AlSiNTs make them amenable to aqueous-phase processing and compatible with soft hydrophilic materials, such as poly(vinyl alcohol).[44] Nevertheless, few of the existing reports discuss the mechanical properties of AlSiNTs.[47-49] The lack of reliable mechanistic research on these mechanical properties has greatly retarded the advancement of AlSiNTs as reinforcing materials for nanocomposites.

Herein, we report on a multiscale computational methodology to investigate the mechanical properties of AlSiNTs based upon the hypothesis that the crystalline structural topology and nanotubular structure could yield higher mechanical strength. We first employ the Cambridge Serial Total Energy Package (CASTEP)[50] to optimize the structure of the atomic model of AlSiNTs. We then compare the potential energy associated with chemical bonds, as estimated from molecular mechanics and the beam strain energy involved in the mechanics of macroscopic materials in order to characterize the covalent bonds in AlSiNTs. These comparisons enable the modeling of covalent bonds (Al-O, Si-O, and O-H) as beam elements in structural mechanics at the macroscopic scale, referred to as nanoscale continuum modeling (NCM).[51] Each chemical bond in the AlSiNTs is then treated as a beam element in simulated tensile, bending, and torsion tests based on mechanics of materials in conjunction with Euler–Bernoulli beam theory. We then deduce the Young's modulus and shear modulus of AlSiNTs of various lengths and diameters based on the results of simulated mechanical tests and compare these values with those of single-walled carbon nanotubes (SWCNTs). To differentiate between the effects of the structural topology and bond strength on the mechanical properties of AlSiNTs and CNTs, we subjected hypothetical nanotubes to the same mechanical tests. Finally, the influence of nanotube structural topologys on mechanical strength is discussed from a quantitative perspective, and guidelines for the design of high-strength nanotube materials are presented.

Results and discussion

Young's modulus of AlSiNTs

Fig. 2 presents the Young's modulus of SWCNTs as well as AlSiNTs of various diameters and lengths, as estimated from simulated tensile tests. The diameter of the AlSiNTs is indicated by the number of unit cells in the circumference, denoted by *N*. AlSiNTs with 11 unit cells in the circumference were denoted as AlSiNT11 and the remainder can be deduced by analogy. AlSiNT11 possesses an external diameter (d_o) of 2.2 nm, and AlSiNT16 possesses a d_o of 3.0 nm. The CNTs discussed in this study are single-walled carbon nanotubes with a chirality of (14,14), denoted as SWCNT (14,14). The Young's modulus of AlSiNTs and SWCNTs remained nearly constant with respect to length in the long-nanotube regime. The observed length effects in the short-nanotube regime is likely due to boundary effects,

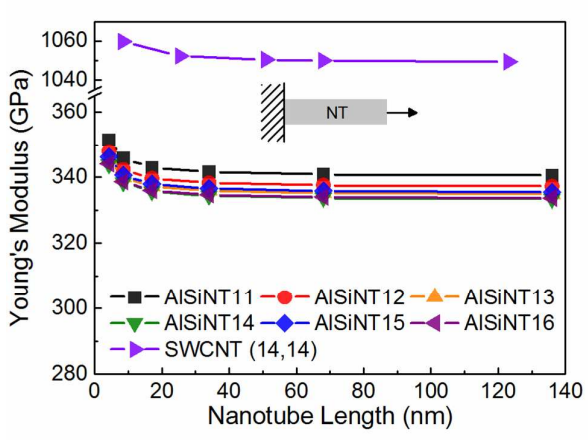

Fig. 2 Young's modulus of AlSiNT11 to 16, and SWCNT (14,14) as a function of nanotube length, which was deduced from simulated tensile tests.

which may become increasingly pronounced with a decrease in the length of the nanotubes.[52] The Young's modulus of AlSiNTs decreased slightly with diameter, likely due to an increase in the hollow regime. In all cases, the Young's modulus of AlSiNTs was approximately 340 GPa, which is higher than that of most engineering materials, such as structural or rail steel (~200 GPa).[53,54] In addition, the Young's modulus of AlSiNTs in this work was consistent with results from previous reports (in a range of 122–479 GPa),[47-49] which was determined by density-functional based tight-binding (DFTB), density functional theory (DFT), or the self-consistent charge density-functional based tight-binding (SCC-DFTB) methods. Nevertheless, the estimations of Young's modulus using the presented nanoscale continuum modelling require much less computational resources than the methods mentioned above. The Young's modulus of SWCNT (14,14) is approximately 1050 GPa, which is in strong agreement with the findings in the previous experimental[26-29] and computational work.[30,31,51] The consistency between our approach and preceding studies with regard to the Young's modulus validates the methodology developed in this work.

Fig. 3 shows the Young's modulus of AlSiNTs and SWCNTs estimated from simulated bending tests. Similar to the results of tensile tests, the Young's modulus of AlSiNTs in the bending tests decreased marginally with an increase in diameter. However, in bending tests, the effect of length on the Young's modulus of AlSiNTs and SWCNTs differed slightly. The convergence of Young's modulus occurred earlier for SWCNTs than it did for AlSiNTs, which implies that SWCNTs are more homogeneous and isotropic than are AlSiNTs. In contrast, the Young's modulus for AlSiNTs in bending tests slightly exceeded the values obtained in tensile tests, which may also be attributed to non-homogeneity and anisotropy caused by the essential discreteness of the model.[55]

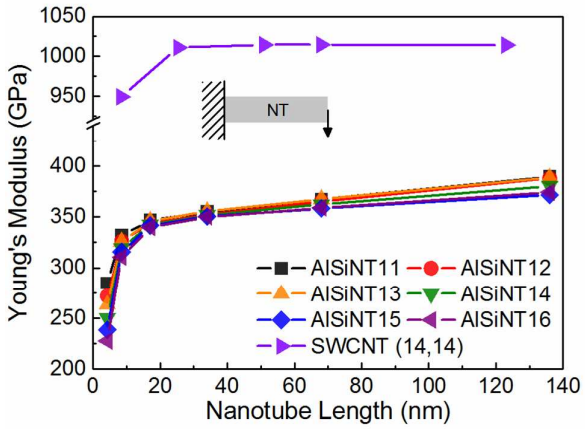

Fig. 3 Young's modulus of AlSiNT11 to 16, and SWCNT (14,14) as a function of nanotube length deduced from simulated bending tests.

Shear modulus of AlSiNTs

Fig. 4 summarizes the shear modulus of AlSiNTs and CNTs estimated from the simulated torsion tests. The shear modulus of long AlSiNTs (length > 30 nm) is approximately 160 GPa whereas the shear modulus of long SWCNTs is approximately 475 GPa. The difference in shear modulus between AlSiNTs and SWCNTs is similar to that of Young's modulus. In the previous experimental[25] and computational[30,31] studies, the shear modulus of SWCNTs was reported to be between 436–478 GPa; however, no reports are available with regard to the shear modulus of AlSiNTs. Unlike the findings from tensile and bending tests, the effects of diameter on shear modulus are nearly undetectable. In other words, the torsional resistance of AlSiNTs remained unchanged regardless of diameter.

It should be noted that the calculated Young's modulus and shear modulus presented above could be affected by changes in nanotube structure based on differences in the criteria for geometry optimization as well as the Poisson's ratio assigned to each beam element in the nanotubes. To validate our method used for the optimization of nanotube geometry, we evaluated the correlation between the level of convergence in geometry optimization and the resulting elastic modulus of nanotubes. The results are summarized in the ESI (Table S1 and Fig. S1†). Our results indicate that the calculated Young's modulus and shear modulus begin converging when the energy tolerance for geometry optimization drops below 10^{-5} eV/atom. Thus, all values related to elastic modulus presented in this study were obtained using AlSiNT models optimized with this criterion. We also examined the degree to which the Poisson's ratio of the beam elements influences the simulation results (Fig. S2†). No notable difference was observed between the calculated Young's modulus and shear modulus in cases with a Poisson's ratio between 0 to 0.5, which is the range of most existing materials,[56] including SWCNTs.[57] Thus, we adopted a Poisson's ratio of 0 for all simulations presented in this work.

Bond strength effects vs. nanotube structural topology effects

As outlined in the preceding section, the Young's modulus and shear modulus of AlSiNTs were both lower than those of CNTs. The difference in the elastic modulus of these two materials may be attributed to the effects of bond strength and nanotube structural topology. Specifically, the carbon-carbon bond in the resonance structure of CNTs is stronger than the Al-O and Si-O bonds in AlSiNTs. Furthermore, the structure of CNTs has nothing in common with that of AlSiNTs. We created two hypothetical nanotubes to evaluate the relative contributions of bond strength and structural topology on the overall mechanical properties. One comprised a CNT structural topology with Al-O bond, and the other comprised an AlSiNT structural topology with carbon-carbon bond. The creation of hypothetical nanotubes for simulated mechanical tests cannot be easily implemented using other computational approaches, such as DFT or molecular dynamics (MD). These two hypothetical nanotubes were then subjected to tensile tests in order to determine the Young's modulus (Fig. 5). The Young's modulus of the hypothetical AlSiNTs comprising carbon-carbon bonds is approximately 70 GPa higher than that of AlSiNTs. Nonetheless, there remains a large gap (approximately 640 GPa) between the hypothetical AlSiNTs

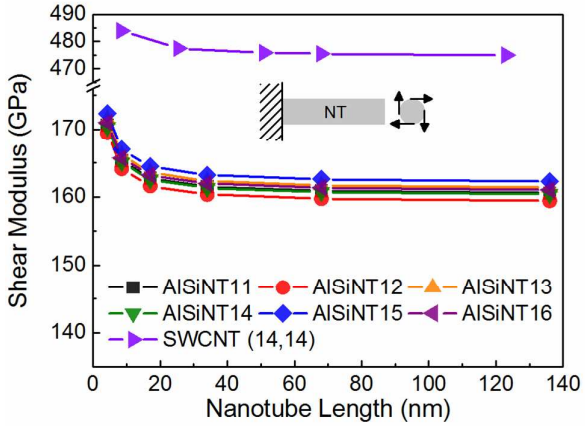

Fig. 4 Shear modulus of AlSiNT11 to 16, and SWCNT (14,14) as a function of nanotube length deduced from simulated torsion tests.

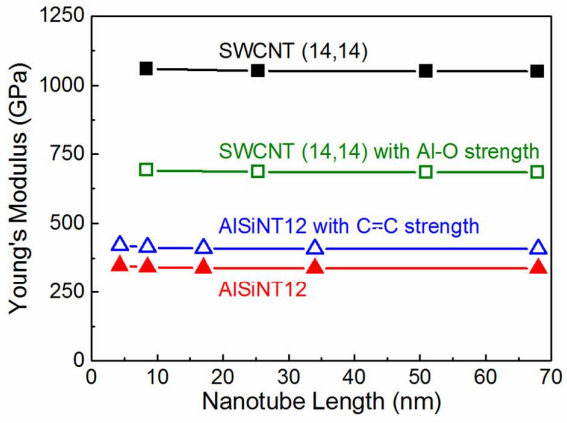

Fig. 5 Young's modulus of two realistic (solid symbols) and two hypothetical (open symbols) nanotubes as a function of nanotube length, as deduced from simulated tensile tests.

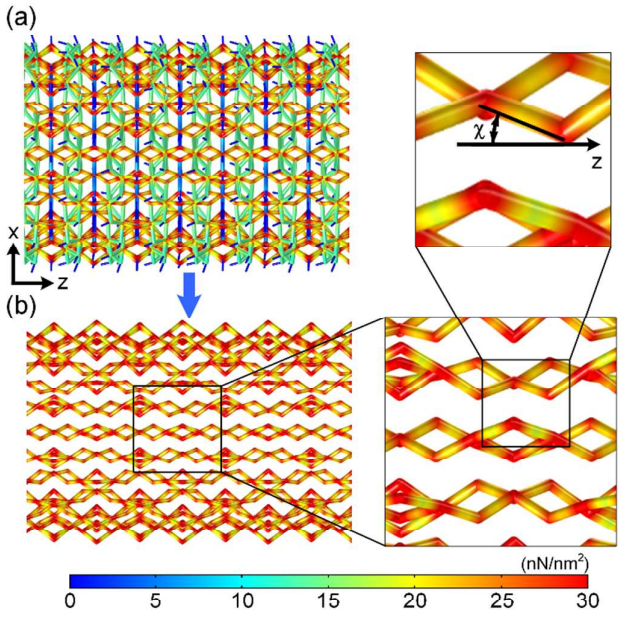

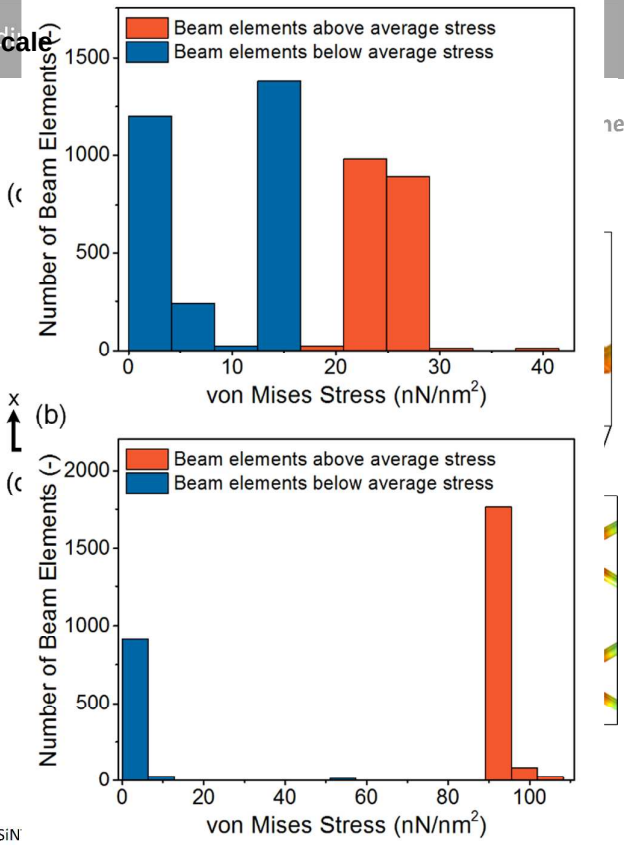

Fig. 6 von Mises stress distribution of (a) AlSiNT12 with all beam elements displayed, (b) AlSiN SWCNT (14,14) with all beam elements being displayed, and (d) SWCNT (14,14) with beam elements of von Mises stress beyond average being displayed. These distributions were obtained using the tensile tests described in the preceding section. χ in the insets denotes the acute angle between the beam element and z-axis.

Fig. 7 von Mises stress distribution: (a) AlSiNT12 (length = 8.5 nm) and (b) SWCNT (14,14) (length = 8.368 nm).

and realistic SWCNTs. A similar trend was observed when we compared the Young's modulus of hypothetical and realistic SWCNTs and AlSiNTs. These results obtained by this unique method suggest that the structural topology plays a more important role than does bond strength in determining the Young's modulus of nanotubes.

Relationship between nanotube structure and mechanical properties

The nanoscale modelling also allows for the detailed investigation of relative contributions of different bonds to the overall nanotube mechanical properties. In the preceding section, we elucidated the impact of nanotube microstructure on the mechanical properties. To gain further insight into the relationship between nanotube structural topology and mechanical properties, we recorded the von Mises stress distributions of nanotubes while undergoing tensile tests (Fig. 6). von Mises stress is a scalar proportional to the square root of the second deviatoric stress invariant, which can serve as an indicator of the point at which a material under stress would yield. Differences between Fig. 6a and 6b and differences between Fig. 6c and 6d indicate beam elements that provide main contributions to the tensile strength of the entire nanotube.

Figs. 7a and 7b summarize the population of all the beam elements under various von Mises stress values in order to facilitate a more quantitative analysis. SWCNT (14,14) presents bimodal distribution whereas the von Mises stress distributions of AlSiNT12 are poorly defined. As for the structural mechanics, only the beam elements subjected to high stress levels contribute to the overall resistance against tension force. Thus, we identified the population of beam elements with above-average von Mises stress at various orientation angles (χ) with respect to the z-axis (Figs. 8a and 8b). Thus, χ serves as an indicator of the degree to which a beam element contributed to the overall tensile resistance of the nanotube. In the ESI (Fig. S3 and S4†), we present the total strain energy and z-component of reaction force in various beam elements as a function of χ, in which strain energy and reaction force both decreased monotonically with χ. This suggested that a beam element oriented at a higher χ might provide a detrimental effect on the overall tensile resistance of nanotubes. It was shown in Figs. 8a and 8b that most high-stress

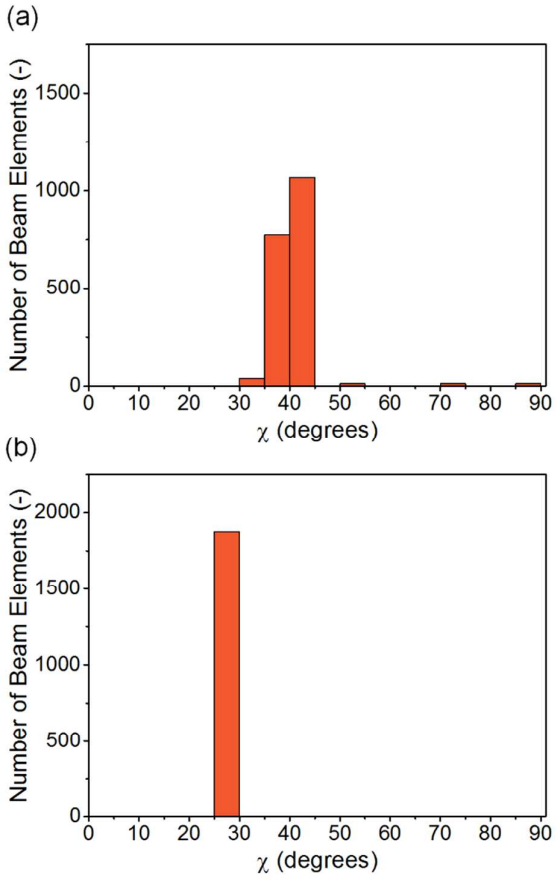

Fig. 8 χ distributions of beam elements with above average von Mises stress in (a) AlSiNT12 (length = 8.5 nm) and (b) SWCNT (14,14) (length = 8.368 nm).

beam elements in SWCNTs are oriented at $\chi < 30^o$, whereas the high-stress beam elements in AlSiNTs are oriented at $30^o < \chi < 45^o$. This may be one of the key reasons that SWCNTs possess a higher Young's modulus (>1000 GPa) than do AlSiNTs (about 340 GPa). To demonstrate that the analysis for AlSiNT12 is representative of AlSiNTs of various diameters, we conducted the same analysis on AlSiNT14 and 16, as summarized in the ESI (Fig. S5†). The stress and χ distributions of AlSiNT14 and 16 are very similar to those of AlSiNT12. A similar relationship between the bond orientation and the mechanical strength of materials has been discussed in SWCNT[58] and graphene[59] systems. In particular, SWCNTs of the armchair type ($\chi = 30^o$) has slightly a higher Young's modulus than those of the zigzag type ($\chi = 60^o$). This supports our finding that the bond orientation χ is one of the dominating factors of the mechanical strength of materials.

Conclusions

This study developed a multiscale computational methodology, involving density functional theory, molecular mechanics, and structural mechanics, to evaluate the mechanical properties of nanotube materials and determine the basis of their mechanical strength. Specifically, we calculated the Young's modulus and shear modulus of single-walled aluminosilicate nanotubes (AlSiNTs) with various diameters and lengths, and then compared these values with those of single-walled carbon nanotubes (SWCNTs) with a chirality of (14,14). The elastic modulus of AlSiNTs was shown to be approximately one third that of SWCNTs. Despite the fact that the strength of AlSiNTs does not match that of SWCNTs, the mechanical strength still exceeds that of most common engineering materials. Considering the ease and scalability of synthesizing AlSiNTs,[60,61] they show considerable potential as a reinforcement material. We also sought to identify the reasons for the differences between these two types of nanotube with regard to elastic modulus by creating two hypothetical nanotubes comprising an AlSiNT structural topology with carbon-carbon bonds as well as a SWCNT structural topology with Al-O bonds. A comparison of hypothetical and realistic nanotubes subjected to the same mechanical tests revealed that the structural topology has a more pronounced effect on mechanical properties than does bond strength. This finding prompted us to investigate the nanotube-structural topology relationship by analyzing the von Mises stress distributions in nanotubes as well as the reaction force response of beam elements as a function of χ, which represents the acute angle of the beam element (covalent bond) with respect to the z-axis. Our findings suggest that chemical bonds more closely oriented to the z-direction would result in higher tensile resistance in the same direction. The methodology developed in this work could be applied to the analysis of other emerging high-strength materials based on nanotubes.

Methods

Construction of nanotube models

A crystal model of gibbsite ($Al(OH)_3$) was first built in accordance with the results reported in a previous study.[62] The hydroxyl of gibbsite ($Al(OH)_3$) on one side was replaced by (SiO_3)OH to create the unit cell of $Al_4Si_2O_{14}H_8$. *N* unit cells of $Al_4Si_2O_{14}H_8$ were then artificially assembled along the circumference to create unit cell models of aluminosilicate nanotubes (AlSiNTs) with an axial repeat distance of 0.85 nm.[35] This study focused on AlSiNT models with $N = 11$ to 16. The structure of each AlSiNT unit cell model was optimized using density functional theory (DFT) with the generalized gradient approximation (GGA) in the scheme of Perdew–Burke–Ernzerhof (PBE).[63] The DFT calculations were implemented using Cambridge Serial Total Energy Package (CASTEP)[50] with an energy tolerance of 10^{-5} eV/atom, a maximum force of 0.03 eV/Å, and a maximum displacement of 10^{-3} Å. A plane wave cutoff energy of 340 eV and 1×1×3 Monkhorst–Pack[64] *k*-point meshes were used for all calculations. The optimized unit cell models were assembled along z-direction to create AlSiNT models with targeting lengths. The fact that the structure of SWCNT (14,14) is well-known made it possible to obtain the model directly from the materials library in Materials Studio®. The atomic coordinates

of the AlSiNT and SWCNT models were used for all subsequent modeling at the nanoscale.

Nanoscale continuum modeling for nanotubes

Nanoscale continuum modeling was applied in simulated mechanical tests on AlSiNTs and SWCNTs in order to obtain their mechanical properties. Nanoscale continuum modeling involves treating the covalent bonds in nanotubes as beam elements in structural mechanics. The mechanical properties of each equivalent beam element, including the Young's modulus and the beam diameter, were determined by equating the potential energy in molecular mechanics with that in mechanics of materials. For molecular mechanics, the total potential energy, U, omitting the electrostatic interaction, involves the contribution of various types of energy:[65]

$$U = \sum U_{\mathrm{r}} + \sum U_{\theta} + \sum U_{\omega} + \sum U_{\tau} + \sum U_{\mathrm{vdW}} \quad (1)$$

where U_{r} is the bond stretching energy, U_{θ} is the energy accounting for the change in bond angle, U_{ω} is the energy associated with dihedral angle torsion, U_{τ} is the energy involved in improper torsion, and U_{vdW} is the energy in non-bonded van der Waals interactions. Fig. S6† presents illustrations of each type of energy. To simplify calculations, we considered only bond stretching and bond angle energy.[30] The bond stretching energy is described in harmonic form:

$$U_{\mathrm{r}} = \frac{k_{\mathrm{r}}}{2}(\Delta r)^2 \quad (2)$$

where k_{r} is the force constant for bond stretching and Δr is the change in bond length. Bond angle energy is expressed in a similar manner:

$$U_{\theta} = \frac{k_{\theta}}{2}(\Delta\theta)^2 \quad (3)$$

where k_{θ} is the force constant in bond angle bending and $\Delta\theta$ is the change in bond angle. Harmonic force constants k_{r} and k_{θ} were obtained from the consistent-valence force field (CVFF).[66]

In contrast, in mechanics of materials, the strain energy of a beam involves the contribution of stretching as well as bending energy. Stretching energy is expressed as

$$U_{\mathrm{A}} = \frac{E_{\mathrm{b}}A_{\mathrm{b}}}{2l_{\mathrm{b}}}(\Delta l_{\mathrm{b}})^2 \quad (4)$$

where E_{b} denotes the Young's modulus of the beam, A_{b} is the cross-sectional area, l_{b} is the beam length, and Δl_{b} is the axial stretching deformation. The bending strain energy is expressed as[30]

$$U_{\mathrm{M}} = \frac{E_{\mathrm{b}}I_{\mathrm{b}}}{2l_{\mathrm{b}}}(2\alpha)^2 \quad (5)$$

where I_{b} denotes the moment of area and 2α is the angle of rotation. In accordance with the methods outlined in previous studies,[30,52,67] eqn (2) and (4), and eqn (3) and (5) could be simultaneously equated for the estimation of E_{b}, A_{b}, and I_{b}, as well as the diameter (d_{b}) of various beam elements, under the assumption of circular beams for the modeling of Al-O, Si-O, and O-H bonds. The mechanical properties of carbon-carbon beam elements were obtained directly from the literature.[52] The parameters for Al-O, Si-O, O-H and carbon-carbon beam elements are summarized in Table S2†.

Simulated mechanical tests

We combined the atomic coordinates of AlSiNT and SWCNT models with the mechanical properties of each beam element for nanoscale continuum modeling and then simulated mechanical tests (tensile, bending, and torsion tests) on the nanotubes, as shown in Fig. S7†. To simulate tensile testing, one end of the nanotube was fixed and axial displacement w_{NT} was applied to the other end (Fig. S7a†). To simulate bending tests, one end of the nanotube was fixed and transverse displacement u_{NT} was applied to the other end (Fig. S7b†). To simulate torsion tests, one end of the nanotube was fixed and displacement was applied in the azimuthal direction around the z-axis, $R\varphi$, where φ is the twist angle (Fig. S7c†). Due to the degree of linearity in the mechanical properties of the tested nanotubes, the amount of displacement applied in all tests was arbitrary. All simulated mechanical tests were performed based on Euler–Bernoulli beam theory using COMSOL Multiphysics® package.

The Young's modulus of nanotubes subject to tensile testing was calculated from the simulation results using the following equation:

$$E_{\mathrm{NT}} = \frac{F_{\mathrm{z}}L_{\mathrm{NT}}}{w_{\mathrm{NT}}A_{\mathrm{NT}}} \quad (6)$$

where F_z is the z component of the reaction force at the fixed end, L_{NT} is the length of the nanotube, and A_{NT} is the cross-sectional area of AlSiNTs excluding the hollow regime. The Young's modulus of nanotubes subject to a bending test was calculated using the following equation:

$$E_{\mathrm{NT}} = \frac{(\sum_i F_{iz}x_i)L_{\mathrm{NT}}^2}{3I_{\mathrm{NT}}u_{\mathrm{NT}}} \quad (7)$$

where F_{iz} is the z component of reaction force on atom i at the fixed end, x_i is the local x-coordinate of atom i (distance between the atom and the neutral axis), and I_{NT} the second moment of area with respect to the neutral axis, with a value of $\pi(d_{\mathrm{o}}^4-d_{\mathrm{i}}^4)/64$ (d_{o} and d_{i} were the outer and inner diameter of a nanotube respectively; and d_{o} and d_{i} were determined by the coordinates of the hydrogen atoms at the external and interior surface of a nanotube respectively). Finally, the shear modulus of nanotubes subjected to torsion testing can be calculated as follows:

$$G_{\mathrm{NT}} = \frac{(\sum_i T_i)L_{\mathrm{NT}}}{J_{\mathrm{NT}}\varphi} \quad (8)$$

where T_i is the torque applied to atom i at the fixed end and J_{NT} is the polar moment with respect to the z-axis, which is $\pi(d_o^4 - d_i^4)/32$.

Acknowledgements

D.-Y.K. and K.-H.L. acknowledge financial support from the Ministry of Science and Technology (MOST) of Taiwan (NSC102-2218-E-002-015-MY2). N.-T.T. acknowledges the support of MOST, Taiwan (MOST 102–2218-E-009–019-MY2). All authors thank You-Yi Lin for his assistance on the model verification. All authors are grateful to the National Center for High-performance Computing (NCHC) for access to computing facilities. All authors acknowledge Dr. Ting-Yu Wang and the Instrumentation Center at National Taiwan University for the cryo-TEM images.

Notes and references

1 J. T. Hu, T. W. Odom and C. M. Lieber, *Acc. Chem. Res.*, 1999, **32**, 435-445.
2 Y. N. Xia, P. D. Yang, Y. G. Sun, Y. Y. Wu, B. Mayers, B. Gates, Y. D. Yin, F. Kim and Y. Q. Yan, *Adv. Mater.*, 2003, **15**, 353-389.
3 Q. H. Wang, D. O. Bellisario, L. W. Drahushuk, R. M. Jain, S. Kruss, M. P. Landry, S. G. Mahajan, S. F. E. Shimizu, Z. W. Ulissi and M. S. Strano, *Chem. Mater.*, 2014, **26**, 172-183.
4 S. Iijima, *Nature*, 1991, **354**, 56-58.
5 J. N. Coleman, U. Khan, W. J. Blau and Y. K. Gun'ko, *Carbon*, 2006, **44**, 1624-1652.
6 Y. Hou, J. Tang, H. Zhang, C. Qian, Y. Feng and J. Liu, *ACS Nano*, 2009, **3**, 1057-1062.
7 N. M. Iverson, P. W. Barone, M. Shandell, L. J. Trudel, S. Sen, F. Sen, V. Ivanov, E. Atolia, E. Farias, T. P. McNicholas, N. Reuel, N. M. A. Parry, G. N. Wogan and M. S. Strano, *Nat. Nanotechnol.*, 2013, **8**, 873-880.
8 S. Kruss, A. J. Hilmer, J. Q. Zhang, N. F. Reuel, B. Mu and M. S. Strano, *Adv. Drug Delivery Rev.*, 2013, **65**, 1933-1950.
9 Z. W. Ulissi, F. Sen, X. Gong, S. Sen, N. Iverson, A. A. Boghossian, L. C. Godoy, G. N. Wogan, D. Mukhopadhyay and M. S. Strano, *Nano Lett.*, 2014, **14**, 4887-4894.
10 G. S. Hong, J. Z. Wu, J. T. Robinson, H. L. Wang, B. Zhang and H. J. Dai, *Nat. Commun.*, 2012, **3**.
11 A. L. Antaris, J. T. Robinson, O. K. Yaghi, G. S. Hong, S. Diao, R. Luong and H. J. Dai, *ACS Nano*, 2013, **7**, 3644-3652.
12 C. Liang, S. Diao, C. Wang, H. Gong, T. Liu, G. S. Hong, X. Z. Shi, H. J. Dai and Z. Liu, *Adv. Mater.*, 2014, **26**, 5646-+.
13 Y. G. Li, W. Zhou, H. L. Wang, L. M. Xie, Y. Y. Liang, F. Wei, J. C. Idrobo, S. J. Pennycook and H. J. Dai, *Nat. Nanotechnol.*, 2012, **7**, 394-400.
14 Y. Y. Liang, H. L. Wang, P. Diao, W. Chang, G. S. Hong, Y. G. Li, M. Gong, L. M. Xie, J. G. Zhou, J. Wang, T. Z. Regier, F. Wei and H. J. Dai, *J. Am. Chem. Soc.*, 2012, **134**, 15849-15857.
15 A. L. M. Reddy, M. M. Shaijumon, S. R. Gowda and P. M. Ajayan, *J. Phys. Chem. C*, 2010, **114**, 658-663.
16 M. Ganzhorn, A. Vijayaraghavan, S. Dehm, F. Hennrich, A. A. Green, M. Fichtner, A. Voigt, M. Rapp, H. von Lohneysen, M. C. Hersam, M. M. Kappes and R. Krupke, *ACS Nano*, 2011, **5**, 1670-1676.
17 R. H. Baughman, A. A. Zakhidov and W. A. de Heer, *Science*, 2002, **297**, 787-792.
18 S. Ozden, L. H. Ge, T. N. Narayanan, A. H. C. Hart, H. Yang, S. Sridhar, R. Vajtai and P. M. Ajayan, *ACS Appl. Mater. Interfaces*, 2014, **6**, 10608-10613.
19 A. Javey, J. Guo, Q. Wang, M. Lundstrom and H. J. Dai, *Nature*, 2003, **424**, 654-657.
20 J. C. Tsang, M. Freitag, V. Perebeinos, J. Liu and P. Avouris, *Nat. Nanotechnol.*, 2007, **2**, 725-730.
21 M. Ganzhorn, A. Vijayaraghavan, A. A. Green, S. Dehm, A. Voigt, M. Rapp, M. C. Hersam and R. Krupke, *Adv. Mater.*, 2011, **23**, 1734-+.
22 A. Vijayaraghavan, *J. Mater. Chem.*, 2012, **22**, 7083-7087.
23 D. Jariwala, V. K. Sangwan, L. J. Lauhon, T. J. Marks and M. C. Hersam, *Chem. Soc. Rev.*, 2013, **42**, 2824-2860.
24 Z. X. Wang, S. B. Liang, Z. Y. Zhang, H. G. Liu, H. Zhong, L. H. Ye, S. Wang, W. W. Zhou, J. Liu, Y. B. Chen, J. Zhang and L. M. Peng, *Adv. Mater.*, 2014, **26**, 645-652.
25 J. P. Lu, *Phys. Rev. Lett.*, 1997, **79**, 1297-1300.
26 A. Krishnan, E. Dujardin, T. W. Ebbesen, P. N. Yianilos and M. M. J. Treacy, *Phys. Rev. B: Condens. Matter Mater. Phys.*, 1998, **58**, 14013-14019.
27 T. W. Tombler, C. W. Zhou, L. Alexseyev, J. Kong, H. J. Dai, L. Lei, C. S. Jayanthi, M. J. Tang and S. Y. Wu, *Nature*, 2000, **405**, 769-772.
28 M. Nakajima, F. Arai and T. Fukuda, *IEEE Trans. Nanotechnol.*, 2006, **5**, 243-248.
29 Y. Wu, M. Huang, F. Wang, X. M. H. Huang, S. Rosenblatt, L. Huang, H. Yan, S. P. O'Brien, J. Hone and T. F. Heinz, *Nano Lett.*, 2008, **8**, 4158-4161.
30 C. Y. Li and T. W. Chou, *Int. J. Solids Struct.*, 2003, **40**, 2487-2499.
31 C. W. S. To, *Finite Elem. Anal. Des.*, 2006, **42**, 404-413.
32 J.-U. Lee, D. Yoon and H. Cheong, *Nano Lett.*, 2012, **12**, 4444-4448.
33 S.-W. Weng, W.-H. Lin, W.-B. Su, E.-T. Hwu, P. Chen, T.-R. Tsai and C.-S. Chang, *Nanotechnology*, 2014, **25**.
34 S. Mukherjee, V. A. Bartlow and S. Nair, *Chem. Mater.*, 2005, **17**, 4900-4909.
35 S. Konduri, S. Mukherjee and S. Nair, *ACS Nano*, 2007, **1**, 393-402.
36 C. Levard, A. Masion, J. Rose, E. Doelsch, D. Borschneck, C. Dominici, F. Ziarelli and J.-Y. Bottero, *J. Am. Chem. Soc.*, 2009, **131**, 17080-+.
37 W. O. Yah, K. Yamamoto, N. Jiravanichanun, H. Otsuka and A. Takahara, *Materials*, 2010, **3**, 1709-1745.
38 C. Levard, E. Doelsch, I. Basile-Doelsch, Z. Abidin, H. Miche, A. Masion, J. Rose, D. Borschneck and J. Y. Bottero, *Geoderma*, 2012, **183**, 100-108.
39 W. Ma, W. O. Yah, H. Otsuka and A. Takahara, *J. Mater. Chem.*, 2012, **22**, 11887-11892.
40 A. Thill, B. Guiose, M. Bacia-Verloop, V. Geertsen and L. Belloni, *J. Phys. Chem. C*, 2012, **116**, 26841-26849.
41 A. Thill, P. Maillet, B. Guiose, O. Spalla, L. Belloni, P. Chaurand, M. Auffan, L. Olivi and J. Rose, *J. Am. Chem. Soc.*, 2012, **134**, 3780-3786.
42 S. Konduri, S. Mukherjee and S. Nair, *Phys. Rev. B: Condens. Matter Mater. Phys.*, 2006, **74**.
43 J. Zang, S. Chempath, S. Konduri, S. Nair and D. S. Sholl, *J. Phys. Chem. Lett.*, 2010, **1**, 1235-1240.
44 D. Y. Kang, H. M. Tong, J. Zang, R. P. Choudhury, D. S. Sholl, H. W. Beckham, C. W. Jones and S. Nair, *ACS Appl. Mater. Interfaces*, 2012, **4**, 965-976.
45 B. Bonelli, I. Bottero, N. Ballarini, S. Passeri, F. Cavani and E. Garrone, *J. Catal.*, 2009, **264**, 15-30.
46 C. Zanzottera, A. Vicente, E. Celasco, C. Fernandez, E. Garrone and B. Bonelli, *J. Phys. Chem. C*, 2012, **116**, 7499-7506.
47 L. Guimaraes, A. N. Enyashin, J. Frenzel, T. Heine, H. A. Duarte and G. Seifert, *ACS Nano*, 2007, **1**, 362-368.

48 G. Teobaldi, N. S. Beglitis, A. J. Fisher, F. Zerbetto and A. A. Hofer, *J. Phys.: Condens. Matter*, 2009, **21**.
49 M. P. Lourenco, L. Guimaraes, M. C. da Silva, C. de Oliveira, T. Heine and H. A. Duarte, *J. Phys. Chem. C*, 2014, **118**, 5945-5953.
50 S. J. Clark, M. D. Segall, C. J. Pickard, P. J. Hasnip, M. J. Probert, K. Refson and M. C. Payne, *Z. Kristallogr.*, 2005, **220**, 567-570.
51 R. Rafiee and R. M. Moghadam, *Composites, Part B*, 2013, **56**, 435-449.
52 P. Papanikos, D. D. Nikolopoulos and K. I. Tserpes, *Comput. Mater. Sci.*, 2008, **43**, 345-352.
53 Y. Y. Bao, H. F. Zhang, M. Ahmadi, M. A. Karim and H. F. Wu, *Ultrasonics*, 2014, **54**, 867-873.
54 S. S. Jung, Y. B. Lee, B. S. Jeon and S. H. Shin, *J. Korean Phys. Soc.*, 2014, **65**, 1024-1027.
55 X. Guo and T. Zhang, *J. Mech. Phys. Solids*, 2010, **58**, 428-443.
56 H. Gercek, *Int. J. Rock Mech. Min. Sci.*, 2007, **44**, 1-13.
57 G. Dominguez-Rodriguez, A. Tapia and F. Aviles, *Comput. Mater. Sci.*, 2014, **82**, 257-263.
58 R. Rafiee and M. Heidarhaei, *Compos. Struct.*, 2012, **94**, 2460-2464.
59 H. Zhao, K. Min and N. R. Aluru, *Nano Lett.*, 2009, **9**, 3012-3015.
60 D. Y. Kang, J. Zang, E. R. Wright, A. L. McCanna, C. W. Jones and S. Nair, *ACS Nano*, 2010, **4**, 4897-4907.
61 D. Y. Kang, N. A. Brunelli, G. I. Yucelen, A. Venkatasubramanian, J. Zang, J. Leisen, P. J. Hesketh, C. W. Jones and S. Nair, *Nat. Commun.*, 2014, **5**.
62 H. Saalfeld and M. Wedde, *Z. Kristallogr.*, 1974, **139**, 129-135.
63 J. P. Perdew, K. Burke and M. Ernzerhof, *Phys. Rev. Lett.*, 1996, **77**, 3865-3868.
64 H. J. Monkhorst and J. D. Pack, *Phys. Rev. B: Condens. Matter Mater. Phys.*, 1976, **13**, 5188-5192.
65 A. K. Rappe, C. J. Casewit, K. S. Colwell, W. A. Goddard and W. M. Skiff, *J. Am. Chem. Soc.*, 1992, **114**, 10024-10035.
66 P. Dauberosguthorpe, V. A. Roberts, D. J. Osguthorpe, J. Wolff, M. Genest and A. T. Hagler, *Proteins: Struct., Funct., Genet.*, 1988, **4**, 31-47.
67 G. M. Odegard, T. S. Gates, L. M. Nicholson and K. E. Wise, *Compos. Sci. Technol.*, 2002, **62**, 1869-1880.